Computational Materials Science 247 (2025) 113546

Contents lists available at ScienceDirect

Computational Materials Science

journal homepage: www.elsevier.com/locate/commatsci

Full length article

# Rapid prediction of the corrosion behaviour of coated biodegradable magnesium alloys using phase field simulation and machine learning

Songyun Ma [a,*], Dawei Zhang [a], Peilei Zhang [b], Bernd Markert [a]

[a] Institute of General Mechanics, RWTH Aachen University, Eilfschornsteinstr. 18, Aachen, 52062, Germany
[b] School of Materials Engineering, Shanghai University of Engineering Science, Longteng Road. 333, Shanghai, 201620, China

ARTICLE INFO

*Keywords:*
Biodegradable magnesium alloy
*In vitro corrosion behaviour*
Coating microstructure
Phase field modelling
Machine learning

ABSTRACT

Surface protective coatings on magnesium alloys have been developed to control the corrosion rate of biomedical magnesium implants under mechano-chemical loadings. Quantifying the effect of coating's microstructural features on the corrosion behaviour of magnesium alloys facilitates the innovative design of biodegradable magnesium implants from the surface to the bulk. The present work is devoted to exploring the applicability of deep learning methods for efficiently predicting the *in vitro* pitting corrosion behaviour of coated magnesium alloys. To this end, the proposed machining learning method employs different CNN models for predicting the corrosion curve and the evolution of corrosion interfaces. In the proposed deep learning method, phase field simulations with varying coating microstructures are used to generate the required corrosion datasets for training and validating the models. The method is applied to a PEO coated WE43 magnesium alloy to assess its feasibility based on *in vitro* experiments. Performance analysis shows that the multi-input CNN is superior to the single-input CNN in predicting the corrosion curve. The proposed encoder–decoder architecture can predict the evolution of corrosion interfaces with an average error about 1%. These results demonstrate that the proposed CNN models provide a promising alternative to conventional simulation methods for evaluating the protective performance of coatings.

## 1. Introduction

Biodegradable magnesium alloys are revolutionary biomedical materials of next generation orthopaedic implants with excellent mechanical performance and biocompatibility. Compared with conventional permanent implants of stainless steels and titanium alloys, biodegradable magnesium orthopaedic implants can be absorbed by human bodies during the bone healing process. The degradation and resorption of magnesium implants avoid a follow-up removal surgery, which significantly reduce patients' risks and considerable socioeconomic burdens on health systems. Nevertheless, their rapid corrosion rates in physiological environments limit their biomedical application in human bodies. An undesired fast degradation of the mechanical integrity can cause a premature failure of implants during the tissue-healing process [1]. In order to control the corrosion rate of biomedical magnesium implants, different surface-modifying approaches have been developed for magnesium alloys, e.g., plasma electrolytic oxidation (PEO) [2], hydrothermal treatment [3], phosphating treatment [4], polymer coating [5] and anodising treatment [6]. The effectiveness of these methods in enhancing the corrosion resistance is critically dependent on their composition, thickness, and microstructure [7–9]. Understanding the structure-performance relationship of coated magnesium alloys, which encompasses multiscale structures from the surface to the bulk, is essential for quantitatively predicting their corrosion behaviour in physiological conditions.

To predict the corrosion behaviour of magnesium alloys under chemomechanical loadings, considerable efforts have been devoted in accessing the corrosion rate and the degradation of mechanical integrity for *in silico* design of magnesium implants. Gastaldi et al. [10] proposed a corrosion model within the framework of continuum damage mechanics to simulate uniform corrosion of magnesium stents. In addition, they coupled a stress corrosion model to the uniform corrosion model for describing the stress assisted corrosion phenomenon. Furthermore, Grogan et al. [11,12] extended the uniform corrosion model to simulate pitting corrosion of biodegradable magnesium alloys observed in *in vivo* experiments. Ma et al. [13] applied an integral-type nonlocal formulation to the pitting corrosion model for overcoming the mesh-dependency of computational results. Recently, the corrosion behaviour of coated magnesium alloys has been studied using numerical methods. Gazenbiller et al. [14] formulated a damage model to

* Corresponding author.
*E-mail address:* ma@iam.rwth-aachen.de (S. Ma).

https://doi.org/10.1016/j.commatsci.2024.113546
Received 11 October 2024; Received in revised form 14 November 2024; Accepted 15 November 2024
Available online 27 November 2024

quantify the effect of PEO coating's microstructure on the mechanical response of magnesium alloys at slow strain rates. Van Gaalen et al. [15] developed experimental and computational methods to evaluate the influence of PEO surface treatments on the corrosion process of a medical-grade magnesium alloy WE43MEO. However, these phenomenological continuum models cannot capture the physical and chemical mechanisms of corrosion, which may lead to a large number of model parameters and inaccurate predictions of the corrosion rate under different immersion conditions. To overcome these limitations of the phenomenological models, physics based continuum models were developed for predicting the corrosion rate of magnesium alloys [16]. Sanz-Herrera et al. [17] proposed a diffusion based model to capture physico-chemical interactions and the evolution of species concentrations during magnesium corrosion. Shen et al. [18] developed a corrosion model for biomedical magnesium alloys to consider corrosion product existence and surface morphology change. Zeller-Plumhoff et al. [19] demonstrated a physics based model to describe the formation/dissolution of corrosion products with realistic compositions of *in vitro* corrosion medium. More recently, phase field methods were applied to simulate the pitting corrosion process of metallic materials [20–22]. This approach can be used for modelling physical and chemical processes involving microstructure evolutions and moving boundaries [23]. Mai et al. [20,24] presented the formulation and implementation of a phase field model for simulating the activation- and diffusion-controlled pitting corrosion phenomena in metallic materials. Kovacevic at al. [25] developed a phase field model accounting for the synergistic effect of aggressive environment and mechanical loading in accelerating corrosion kinetics of magnesium alloys. Zhang et al. [26] presented an energetic variational framework for modelling deformation-fracture-corrosion interactions in the corrosion process of magnesium alloys. However, simulating microstructural evolutions with phase field models demands significant computational cost, regardless of different time-integration methods [27] and implementations of parallel computation [28].

To efficiently predict the corrosion behaviour of metallic alloys, machine learning methods have been considered as an alternative promising approach in the last years [29]. A multilayer perceptron (MLP) can lead to much lower computational time and can replace the mathematical model according to designed algorithms [30]. It can be trained by feeding experimental data or simulation results. In general, the MLP can be seen as an approximator of the existing data. As the existing data cover the possible data space, the well-trained MLP has the ability to predict the result for a new input. Furthermore, convolutional neural network (CNN) has achieved significant success in image classification, object detection and image segmentation [31]. Therefore, CNN has been utilised to solve various problems in science and engineering, e.g. predicting the evolution of stress fields [32], detecting effective diffusivity of porous media [33], optimising the mechanical properties pf composites [34], seeing permeability from images [35] and predicting 3D microstructure-sensitive fatigue crack [36]. Especially, 1D CNNs have shown high effectiveness in predicting time- and path-dependent material behaviours, such as calculating retention curves for porous media [37]. Recent studies have attempted to apply machine learning methods for predicting the corrosion behaviour of magnesium alloys [38]. Moses et al. [39] utilised a machine learning model to predict the effect of chemical compositions and environmental factors on the corrosion potential and corrosion current of magnesium alloys. Schiessler et al. [40] proposed sparse machine learning models to analyse the corrosion inhibition efficiency of chemical compounds for magnesium alloys. Wang et al. [41] developed a high-throughput computational strategy based on first-principles calculations and machining learning models to investigate the corrosion behaviour of binary magnesium alloys with intermetallics for the corrosion-resistant magnesium alloy design. Maqbool et al. [42] combined virtual sample generation and machine learning approaches to predict corrosion rates of friction stir processed magnesium alloys with different processing parameters. Nevertheless, very limited studies focus on the machine learning based model to predict the structure-performance relationship of coated magnesium alloys, which plays an important role in *in silico* design of coated biodegradable implants.

This work is therefore devoted to explore the applicability of deep learning methods for rapid predictions of the corrosion curve and the corrosion interface of coated magnesium alloys. Within the deep learning framework, phase field simulations with varying coating microstructures are used to generate the required datasets of corrosion for training and validating the CNN models. The proposed machining learning method employs different CNN models for predicting the corrosion curve and the evolution of corrosion interfaces. In the case of predicting the corrosion curve, the conventional CNN architecture processes images through a combination of a sequence of convolutional and polling layers followed by a fully connection layer. The second machining learning model for this purpose modifies the connection between input and the fully connected layer, three physical quantities of coating's microstructure directly are integrated into the dense layer. In the case of the corrosion interface prediction, an encoder–decoder architecture is applied. Encoder reduces the input image to a feature vector and decoder produces the corrosion interface from the feature vector. This framework was validated with a dataset of a PEO coated magnesium alloy WE43MEO, comprising 2600 samples of diverse microstructures to train and validate the deep learning models. Various filter sizes and convolutional layers were explored during the cross-validation process to identify the optimal hyperparameters for the neural networks. A performance analysis demonstrates that the multi-input CNN has in general superior prediction accuracy compared to the conventional single-input CNN. Compared to FEM simulations, the well-trained multi-input CNN model and encoder–decoder model can provide a prediction in seconds with an average relative error of 0.5% and 1%, respectively.

## 2. Deep-learning framework

The CNN based deep learning framework is designed for a rapid estimation of the corrosion curve and the corrosion interface of coated magnesium alloys. Due to the limited experimental data for the coating microstructure and the *in vitro* corrosion behaviour of PEO-coated magnesium alloys, we generate the microstructure of PEO coatings by considering the main features of defects in the PEO coating and use the corrosion data predicted by the validated phase field simulations for training the developed CNN models. In further work, the direct experimental dataset can be included in the training process as more experimental results of PEO coated magnesium alloys are available. This section provides a brief introduction to the data generation algorithm, and the architecture of the used CNN models.

### 2.1. Overview of the computational framework

The aim of this computational framework is to develop machine learning models for a rapid prediction of corrosion behaviours, encompassing the corrosion curve and the corrosion interface, as shown in Fig. 1. The key steps of this framework are explained as follows:

(i) *Generating dataset.* The initial step involves the creation of a diverse dataset by generating numerous microstructures of coating based on a randomised algorithm. Phase field simulation is then used to generate the corrosion curve and the evolution of the corrosion interface (pit morphology) for each coated alloy.

(ii) *Training deep learning models.* The data generated in the previous stage is utilised to train neural networks with various architectures, demonstrated in Fig. 1. For predicting the corrosion curve, two types of CNN are compared. The first is the single-input CNN (SICNN), which adopts a classic CNN architecture and solely takes images of coating microstructures as

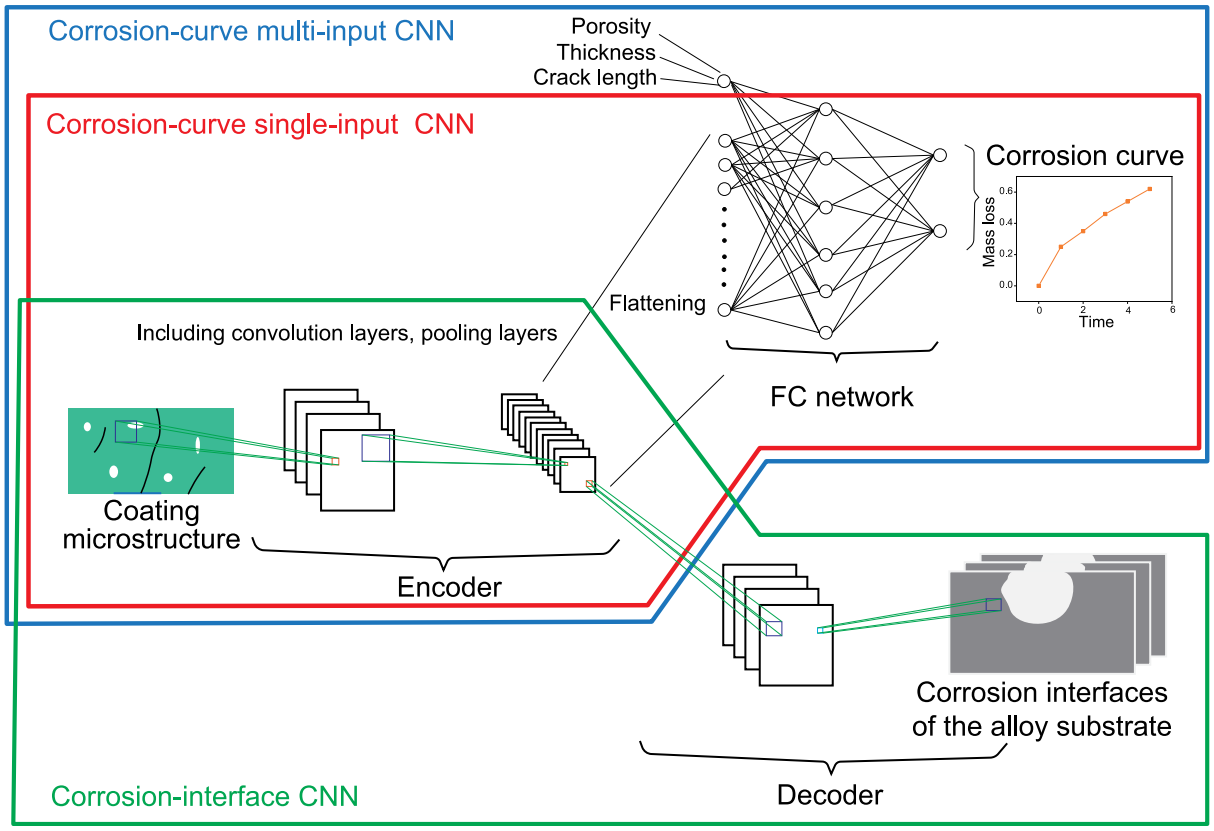


**Fig. 1.** Schematic of the proposed CNN architectures. The corrosion-curve single-input CNN is composed of an encoder and a FC network, taking only the coating image as input. The corrosion-curve multi-input CNN integrates structural parameters into the feature vector produced by the encoder, extending this vector before passing it to the FC network. The corrosion-interface CNN employs an encoder–decoder architecture to generate corrosion morphologies directly from coating images.

input. The second is a novel CNN, referred to as the multi-input CNN (MICNN), that incorporates structural parameters of coating as additional inputs. For predicting the corrosion interface, the encoder–decoder architecture [43–45] is employed. This corrosion-interface CNN (CICNN) outputs a three-dimensional tensor comprising interface images for various corrosion periods. The encoder is responsible for feature extraction from the images, while the decoder generates the corrosion interface images from coating features.

(iii) *Predicting the corrosion behaviour of magnesium alloy-coating system.* The trained models from step (ii) are subsequently applied to predict the corrosion behaviour for magnesium alloy-coating system in the validation set.

### 2.2. Neural networks for predicting corrosion behaviour

Currently, multilayer perceptron and convolutional neural network are two main types of artificial neural networks. MLP builds nonlinear mapping from input $\mathbf{x}$ to output $\mathbf{y}$ via a sequence of functions parametrised by the weight vector $\mathbf{W}$, bias vector $\mathbf{b}$ and activation function $\sigma$. For each layer, the relation between input and output is represented by:

$$\mathbf{y}^{(l)} = \sigma\left(\mathbf{W}\mathbf{x}^{(l)} + \mathbf{b}^{(l)}\right), \tag{1}$$

and the relation $\mathbf{x}^{(l+1)} = \mathbf{y}^{(l)}$ applies for the next layer. In the most general form, MLP can be considered as a function approximator. Due to inherent architectural constraints, MLP typically takes compact data as inputs. When processing a large volume of data, both computation time and memory requirements can increase dramatically. To enhance the high-dimensional data processing capability of neural networks, convolution layers that leverages the advantage of local receptive fields and weight-sharing properties have been integrated into neural networks [46,47]. The convolutional layer performs convolutional operations on the input channels and transmits the results to the subsequent layer. Consequently, CNN can extract distinguishing features from the input data through the scanning and convolutional operations facilitated by various filters/kernels. For a two-dimensional input image $\mathbf{X}$ and a two-dimensional convolution kernel $\mathbf{K}$, the output $\mathbf{Y}$ is expressed as [47]:

$$\mathbf{Y}^{(l)}(i,j) = \sigma\left(\sum_m \sum_n \mathbf{X}^{(l)}(i+m, j+n)\mathbf{K}^{(l)}(m,n)\right), \tag{2}$$

where $i$ and $j$ are the pixel indices of the output in two dimensions, $m$ and $n$ are weight indices of the kernel.

In this study, MLP models were constructed to assess the feasibility of predicting corrosion curves from structural parameters and used as a benchmark for evaluating the neural network performance prior to designing CNN models. In the coated magnesium alloys, the corrosion behaviour of substrate is mainly affected by three microstructural parameter, porosity, coating thickness, and the initial crack length of passive film. Their effects on the degradation process of magnesium alloys were explicitly integrated into the neural network in a flexible and clear manner. This network architecture embodies our prior knowledge that the corrosion depth might be a function of these microstructural parameters, although the specific functional relationship is unknown and must be established through training. Different configurations of hidden layers and hidden units are tested to strike a balance between accuracy and efficiency. While the corrosion curve may indeed be a function of the three structural parameters, it can also be influenced by other factors, such as the position of pores. Additionally, the morphology of corrosion pits, which is crucial for assessing the integrity of the alloy, cannot be accurately obtained through a few statistical

parameters of the coating microstructure. This raises the necessity of using coating images as input.

The encoder in the CNN models captures microstructure information from coating images through a series of convolutional and pooling layers, processing the raw coating image into a set of feature representations. For classification or regression tasks, the feature tensor is typically flattened into a vector by the dense layer for further processing. In the corrosion-curve CNN models, the feature vector is then forwarded to the FC network, which is supposed to have the same architecture as the aforementioned MLP, to predict the data points on the corrosion curve. Additionally, the single-input CNN can be extended by incorporating the three structural parameters into the one-dimensional feature vector, as shown in Fig. 1. This extended CNN architecture is referred to as the multi-input CNN, given its input consisting of both image and structural parameters. The CNN model for predicting the corrosion interface is structured according the encoder–decoder architecture [43–45]. The encoded coating feature information is restructured by the decoder which uses a series of transposed convolutional operations to upsample the features and produce the corrosion morphologies. The proposed three CNN models share the same encoder architecture and their overall schematic of architectures is depicted in Fig. 1.

### 2.3. Model optimisation and evaluation

The common learning algorithm calculates the gradients of the loss function $J$ with respect to the network hyperparameter vector $\Theta$ by backpropagation [48], and obtains the optimal $\Theta$ via optimisers, such as the gradient descent algorithm

$$\Theta_{i+1} = \Theta_i - \alpha \frac{\partial J}{\partial \Theta_i}, \tag{3}$$

where $\alpha$ indicates the learning rate. $\Theta_i$ and $\Theta_{i+1}$ represent hyperparameters of the network in the $i$th and $(i+1)$th epoch, respectively. The generated coating samples are fed into the neural network models in mini-batches of several images with the associated corrosion data. To prevent the learning process from getting stuck in local minima and being affected by the data sequence, the training set is shuffled. In this study, the mean square error (MSE) is used as the loss function to calculate the deviation between the prediction of the mini-batch and its ground truth

$$\mathrm{MSE} = \frac{1}{M \times N} \sum_{j=1}^{M} \sum_{i=1}^{N} \left( y_{i,j}^{P} - y_{i,j}^{G} \right)^2, \tag{4}$$

where $M$ and $N$ indicate the number of coating samples encapsulated in a mini-batch and the number of entities in each corrosion curve/interface set, respectively. $y_{i,j}^{P}$ is the $i$th entity of the $j$th predicted corrosion curve/interface set, while $y_{i,j}^{G}$ is the corresponding ground truth.

To evaluate the prediction performance, the mean absolute error (MAE) and the mean relative error (MRE) are implemented. For each predicted result, the MAE is defined by:

$$\mathrm{MAE} = \frac{1}{N} \sum_{i=1}^{N} \left| y_i^P - y_i^G \right|, \tag{5}$$

where $N$ denotes the number of entities in the output data, $y_i^P$ and $y_i^G$ are the $i$th entity of the predicted corrosion curve/interface set and the corresponding ground truth, respectively. The relative error of each corrosion curve is defined by:

$$\mathrm{MRE}_{\mathrm{curve}} = \frac{1}{N} \sum_{i=1}^{N} \frac{\left| y_i^P - y_i^G \right|}{y_i^G}. \tag{6}$$

Because the ground truth matrix of the corrosion interface contains zero values, the following formulation of MRE is defined for corrosion-interface CNN models to avoid a zero in the denominator [45]:

$$\mathrm{MRE}_{\mathrm{interface}} = \frac{MAE}{\max \left\| y^G \right\| - \min \left\| y^G \right\|} \times 100\%, \tag{7}$$

where $\max \left\| y^G \right\|$ and $\min \left\| y^G \right\|$ denote the maximum and minimum values from the ground truth matrix, respectively.

## 3. Application to PEO coated magnesium alloy we43MEO

### 3.1. Materials and in vitro corrosion experiment

For the *in vitro* corrosion experiments, round test specimens with a diameter of 4 mm were fabricated by Medical Magnesium GmbH (Aachen, Germany) from 9.5 mm rods of clinically used extruded magnesium rare-earth alloy WE43MEO (Meotec GmbH, Aachen). The alloy is manufactured considering the following elemental specifications: 1.4 – 4.2 wt% Y, 2.5 – 3.5 wt% Nd, < 1 wt% for Al, Fe, Cu, Ni, Mn, Zn, Zr and Mg as balance. A second test group of WE43MEO specimens was coated with plasma electrolytic oxidation (PEO). The PEO surface modification was conducted in a phosphate based electrolyte by using a pulsed rectifier set (M-PEO A1, Meotec GmbH, Germany). The process parameters were galvano-statically adjusted starting at 10 $\mathrm{A/m^2}$ to produce an evenly distributed coating on the substrate with the average thickness of 20 μm [49]. The samples were wrapped with Teflon tape at both ends and sealed with heat shrink tubing to prevent corrosion. Therefore, only the central parallel region of the samples with the length 24 mm was exposed to the corrosion environment. The microstructures of the samples are presented in Fig. 2. The morphology of the coating reveals a typical porous structure with both interconnected and isolated pores. The immersion tests for a period up to 28 days were conducted in an incubator at 37 °C with 7% $CO_2$ for ideal pH buffering of the fluid. To simulate the physiological environment with the similar ionic compositions of blood plasma, we used the cell culture medium DMEM (L0101-500, Biowest, Nuaillé, France) composed of inorganic and organic compounds. The DMEM contains phenol red as a colour indicator for visual control of the physiological regime of pH value [50]. Fig. 3 shows SEM images of the corrosion morphology of coated WE43MEO samples after immersion periods of 7 and 28 days.

The hydrogen gas evolving during corrosion was collected via an inverted funnel placed on top of the specimen into a burette which allows a time-dependent measurement of the corrosion rate. The mass loss per area of magnesium alloy $\Delta M$ ($\mathrm{mg/cm^2}$) can be further evaluated by the collected volume of hydrogen gas $V_{\mathrm{H}}$ (mL) according to the relationship [51]:

$$\Delta M = P M_{\mathrm{Mg}} V_{\mathrm{H}} / (R T A) \tag{8}$$

with the gas pressure $P$ (1 atm), molar mass of magnesium $M_{\mathrm{Mg}}$ (24310 mg/mol), molar gas constant $R$ (82.05 mL atm $\mathrm{K^{-1} \cdot mol^{-1}}$), temperature $T$ (310.15 K) and surface area $A$ (3.016 $\mathrm{cm^2}$).

### 3.2. Phase field model for pitting corrosion in WE43MEO

Magnesium alloys exposed to an aqueous environment form a passive MgO layer on the surface that protects the magnesium alloy matrix from corrosion. However, if the passive film is too thin or completely cracked in certain regions, the solution directly contacts the freshly exposed alloy substrate in those areas, leading to the formation of pits. Under *in-vitro* or *in-vivo* conditions, chemical reactions occurring on the unprotected surface of magnesium alloys lead to the formation of a stable corrosion product layer consisting of various corrosion products. This growing layer on biodegradable magnesium alloys hinders water access to the alloy matrix and impedes the transport of ions in the long-term corrosion process [52].

Herein, we consider a mixing domain of magnesium alloy and the electrolyte $\Omega \in \mathcal{R}^3$ with the external boundary $\partial\Omega$, which is decomposed into the solid boundary $\partial\Omega_s$ and the electrolyte boundary $\partial\Omega_l$ with $\partial\Omega = \partial\Omega_s + \partial\Omega_l$ and $\partial\Omega_s \cap \partial\Omega_l = \varnothing$. In the present phase field model, we introduce an auxiliary variable $\phi$ to indicate the material state with $\phi = 0$ being the totally corroded material and $\phi = 1$ being the uncorroded alloy matrix. The boundary conditions for the

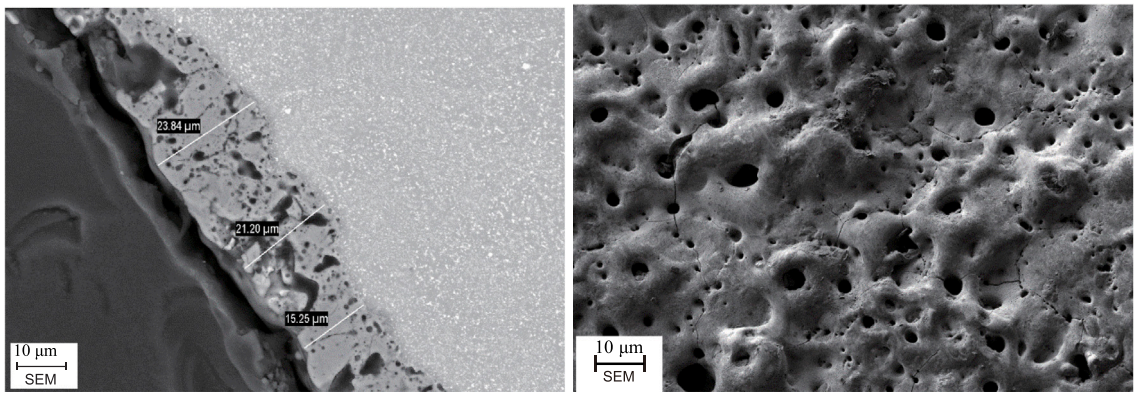


**(a)** Cross-sectional morphology **(b)** Surface morphology

**Fig. 2.** Microstructures of the PEO coating on WE43MEO.

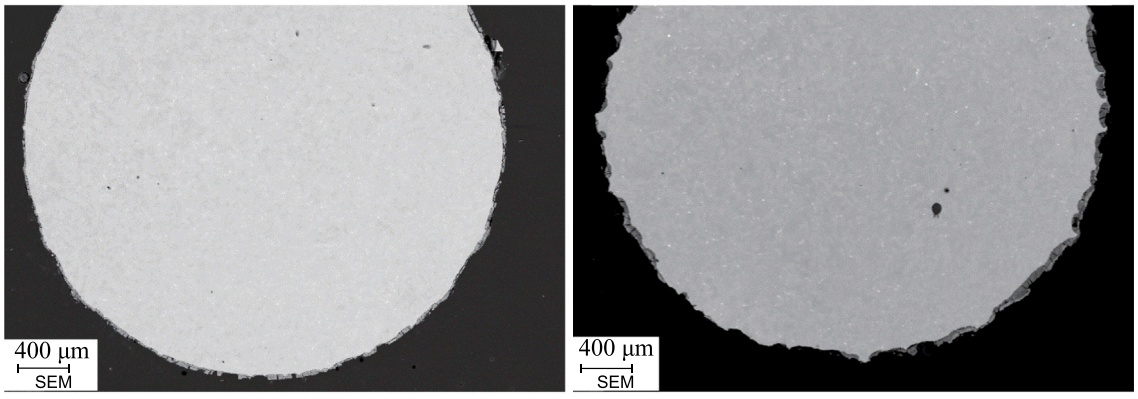


**(a)** 7 days **(b)** 28 days

**Fig. 3.** Cross-sectional corrosion morphologies of PEO coated WE43 specimens.

corrosion phase field are $\phi = 0$ on $\partial\Omega_l$ and $\nabla\phi \cdot \boldsymbol{n} = 0$ on $\partial\Omega_s$. The Mg ion concentration field of the domain is defined by introducing the normalised ion concentration $c^*(\boldsymbol{x}, t) = c(\boldsymbol{x}, t)/c_{\text{solid}}$, where $c_{\text{solid}}$ is the equilibrium concentration of ions in the solid. The flux of ions is driven by the chemical potential $\mu$.

The governing equations of the phase field model are derived by taking the stationarity of the rate-type potential functional $\Pi$ detailed in [26], which yields

$$\delta_\phi \Pi : \dot{\phi} = -L\left(\frac{\partial \psi}{\partial \phi} - r_c\right), \tag{9}$$

$$\delta_\mu \Pi : \dot{c}^* = \nabla \cdot M \nabla \mu, \tag{10}$$

$$\delta_{c^*} \Pi : \mu = \frac{\partial \psi}{\partial c^*} - \nabla \cdot \frac{\partial \psi}{\partial \nabla c^*}, \tag{11}$$

where $L$ is the interface kinetics parameter and $M$ is the diffusion mobility of ion transport. $r_c$ is the corrosion resistance and defined by

$$r_c := \alpha_c \nabla \cdot \nabla\phi - \omega_c \partial_\phi g_w(\phi), \tag{12}$$

where $\alpha_c$ is the gradient energy coefficient associated with the phase field $\phi$. $g_w(\phi) = \phi^2(1-\phi)^2$ is the double well potential and $\omega_c$ is the height of the imposed double-well energy barrier. The free energy density $\psi$ is expressed as a function of the corrosion phase field $\phi$ and the normalised ion concentration $c^*$,

$$\psi(c^*, \phi, \nabla c^*) = A\left[c^* - \left(1 - h_c(\phi)\right) c^*_{Le} - h_c(\phi) c^*_{Se}\right]^2 + \kappa \nabla c^* \cdot \nabla c^*, \tag{13}$$

where $A$ is the free energy density curvature and $h_c(\phi) = -2\phi^3 + 3\phi^2$ is an interpolation function for ions concentrations in both phases. $c^*_{Le}$ and $c^*_{Se}$ are the normalised equilibrium concentration in the corroded material and alloy matrix. $\kappa$ is the concentration gradient energy coefficient [53] and assumed to be 0, as suggested by [54]. Then, the governing equation for ion concentration Eq. (11) is reduced to a local equation as

$$\mu = 2Ac^* + 2A(c^*_{Le} - 1)(3\phi^2 - 2\phi^3) - 2Ac^*_{Le}, \tag{14}$$

and boundary conditions for $\mu$ are then defined as Dirichlet boundary condition $\mu = \bar{\mu}(\boldsymbol{x})$ on $\partial\Omega_l$ and $\partial\mu/\partial\boldsymbol{n} = 0$ on $\partial\Omega_s$, with detailed derivation refer to [26]. Additionally, the diffusion mobility $M$ can determined by the diffusion coefficient $D$ and the free energy density curvature $A$ as $M = \frac{D}{2A}$.

The corrosion of coated magnesium alloys is primarily initiated by discharge channels in the coating and cracks in the passive film [55]. Through these channels and cracks, the electrolyte solution comes into contact with the magnesium alloy matrix. During the initial stage, the channels, cracks, and pores are filled with corrosive medium, in which the diffusion coefficient of magnesium ions is identical to that in the dilute solution ($D_{\text{sol}} = 8.5 \times 10^{-10}$ m$^2$/s [26]). As the corrosion process progresses in physiological media with complex ions and organic components, very complicated mechano-electrochemical processes lead to deposition and accumulation of corrosion products in the microdefects. As a result, these microstructural defects are gradually covered and blocked by the accumulated corrosion products [56–58]. After corrosion products sealing the microdefects, the diffusion coefficient of ions in pores and channels decreases to the value of that in corrosion products $D_{\text{cp}}$. To capture such blocking phenomena, an interpolation between two diffusion coefficients is approximated by

$$D = D_{\text{cp}} + (D_{\text{sol}} - D_{\text{cp}}) e^{-bt}, \tag{15}$$

where $b$ is a evolution coefficient and $t$ is the immersion time with unit in day.

**Table 1**
Parameters of the phase field model calibrated for the WE43MEO alloy.

| Parameter | Physical interpretation | Value |
|---|---|---|
| $A$ | Free energy density curvature | $5.35 \times 10^7$ J/m$^3$ [54] |
| $c_{\text{solid}}$ | Saturated concentration of WE43 | 67.319 mol/L [59] |
| $c^*_{Le}$ | Normalised saturated Mg-ion concentration in the corroded phase | 0.051 [26] |
| $D_{c\text{-cp}}$ | Diffusion coefficient within corrosion product | $1.17 \times 10^{-14}$ m$^2$/s |
| $D_{c\text{-PEO}}$ | Diffusion coefficient within PEO coating | $8 \times 10^{-16}$ m$^2$/s |
| $b$ | Evolution coefficient | 1.7 |
| $L$ | Interface kinetics coefficient | 2 m$^3$/(Js) [54] |
| $\alpha_c$ | Gradient energy coefficient | $5.1 \times 10^{-5}$ N [54] |
| $w_c$ | Height of the double-well energy barrier | $3.528 \times 10^7$ J/m$^3$ [54] |

In this work, the governing equations are solved by the commercial FEM software FlexPDE with cubic (ten-node) triangular elements for discretising the domain. To guarantee the simulation accuracy and the numerical stability, the mesh size is defined such that the interface region contains at least six nodes. The iteration solution approach is the Newton–Raphson method. The maximum iteration step is assigned to be 3 and the Jacobian matrix for each iteration step is recalculated to guarantee the stability.

The calibration of model parameters is achieved through two steps. First, the uncoated model is used to determine the parameters for WE43MEO. Subsequently, the diffusion coefficient of ions within PEO coatings and the evolution coefficient are calibrated using the coated model. The calibrated parameters for PEO coated magnesium alloys are listed in Table 1 using the models shown in Fig. 4. In both models, the thickness of the alloy substrate is determined by assessing the maximum corrosion depth, ensuring that the results are not affected by model boundaries while minimising computational cost. An initial pit is represented by the initial crack in the passive film with the thickness of 2 μm. The size of the initial pit is chosen to be 40% of the total length of the computational model, according to the suggested proportion of broken regions in the passive film for matching the experimental data of *in vitro* corrosion tests in DMEM in [26]. The boundary conditions $\phi = 0$ and $\mu = -2Ac^*_{Le}$ are prescribed along the upper boundary immersed in the electrolyte, while initial conditions are $\mu = 0$, $\phi = 1$ in the alloy matrix, and $\mu = -2Ac^*_{Le}$, $\phi = 0$ in the PEO coating. The coating thickness is 20 μm according to the average thickness identified in the experiments. Pores in the coating with a diameter of 2.6 μm, which is the average size of pores experimentally determined via image analysis, are randomly distributed to achieve the measured porosity of 15.7%. The width of discharge channel is assumed to be 2 μm as the thickness of the passive film. The predicted corrosion curves of the uncoated and coated WE43MEO from the computational results with the calibrated model parameters are illustrated in Fig. 5, which shows a good agreement with the experimental results. The relatively larger deviation between the experimental and computational results for the coated specimen is found in the early stage of corrosion, which may be attributed to the neglect of additional micro-galvanic interactions between the coating and the alloy substrate, leading to an extremely fast initial corrosion rate.

### 3.3. Dataset generation

The microstructural features of the PEO coating are divided into three categories: pore, discharge channel and initial crack in passive film. The geometry and boundary conditions are illustrated in Fig. 6, where the size of each model is 67 × 200 μm. The boundary condition are assigned as: Dirichlet conditions $\phi = 0, \mu = -2Ac^*_{Le}$ in the electrolyte and Neumann conditions $\nabla\phi \cdot \boldsymbol{n} = 0, \boldsymbol{h} = 0$ on the other boundaries. The initial conditions of the alloy matrix and PEO coatings are defined as $\mu = 0, \phi = 1$ and $\mu = -2Ac^*_{Le}, \phi = 0$, respectively. In this study, the microstructures of PEO coatings are generated randomly according to the following principles:

(i) *Coating thickness.* The coating thickness is sampled in the range of 15–30 μm. To maintain a consistent image size for image processing with CNN, an electrolyte region illustrated as the yellow region in Fig. 6 is added to the outside of the PEO coating. Its thickness is adjusted according to the coating thickness.
(ii) *Initial crack in the passive film.* The position of the initial crack is randomly generated in the passive film. Subsequently, the length of the initial crack region is randomly generated between 5–150 μm, and the discharge channel always connects to the initial crack.
(iii) *Pore distribution.* The porosity of the PEO coating is generated between 0 and 30%. Pores with a diameter randomly sampled between 1 and 3 μm are then seeded at random positions until the predefined porosity is achieved.

In this study, all random processes follow uniform distributions. Different microstructural features are represented using different colours, aiding the neural network in distinguishing these features.

Phase field simulations with different coating microstructures are used to generate data in terms of corrosion curves and corrosion interfaces. To simplify the representation of the corrosion curve, we have selected 8 data points that adequately capture the curve's features, including data for Day 1, 2, 3, 4, 7, 14, 21, and 28. The image of the phase field variable distribution is converted into binary images of corrosion interfaces with each pixel representing 1 μm, as depicted in Fig. 7. The dataset encompasses 2600 distinct microstructures of PEO coatings paired with their corresponding corrosion curves and interfaces for training and evaluating deep learning models. For this purpose, 800 samples were allocated for training, 200 samples for testing, and 1,600 samples for evaluating the well-trained models, following a 4:1:8 split.

### 3.4. Impact of microstructures in PEO coatings on the corrosion behaviour of alloy substrates

It is reported that the thickness of the coating and the porosity significantly affect the corrosion resistance of PEO coated magnesium alloys [60]. In this study, we use the phase field simulation to quantify the influence of coating's microstructural features on the corrosion behaviour of alloys substrate. For this purpose, the initial crack in passive film with the length 150 μm is set together with the discharge channel in the middle of the computational model. The diameter of all pores is 3 μm. The discharge channel in the coating allows the solution to contact the alloy substrate, and almost all of the magnesium ions diffuse through the channel into the electrolyte before it is filled with corrosion products. As a result, the coating provides negligible protection during the initial stages of corrosion. Accordingly, the corrosion process of PEO coated magnesium alloys in DMEM can be divided into Phase I (0–4 days) and Phase II (5–28 days) after evaluating the corrosion curves. The average corrosion rate $CR$ mentioned below refers to the mass loss per unit area $\Delta M$ over a specific period, divided by the duration $\Delta t$ of that period, as

$$CR = \Delta M / \Delta t . \tag{16}$$

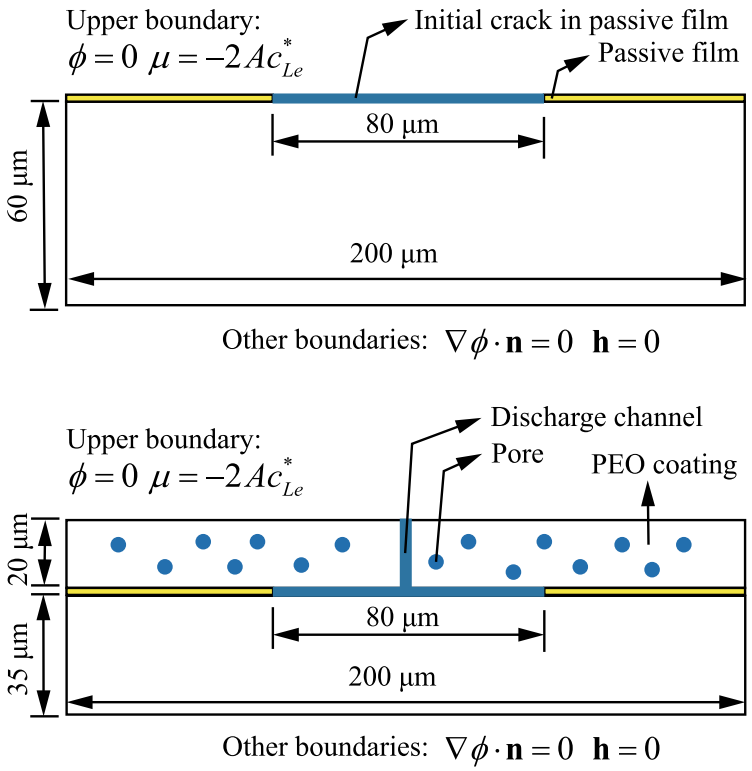


**Fig. 4.** The models and boundary conditions for calibrating the model parameters of the WE43MEO substrate (up) and the PEO coating (down).

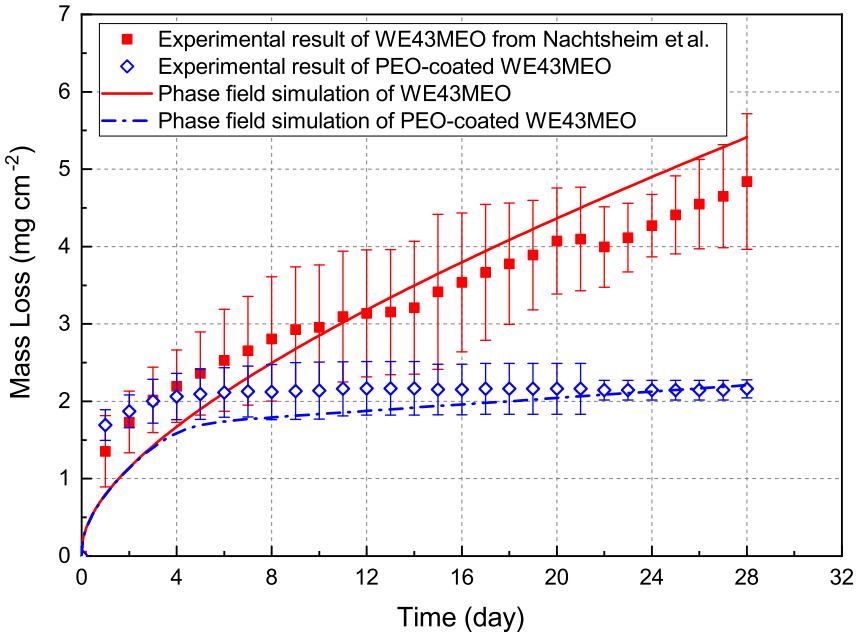


**Fig. 5.** The mass loss per surface area of the non-coated and PEO coated WE43MEO specimens in *in-vitro* experiments [51] and phase field simulations.

The influence of coating thickness and porosity in Phase II is studied as follows:

(i) **The influence of coating thickness.** In these simulations, the porosity is set to be 0.15. As shown in Fig. 9, the corrosion rate decreases with the increase of thickness. Comparing the results for the coatings with the thickness of 15 and 20 μm, the corrosion rate changes from 49.6 to 40.5 μg cm$^{-2}$ d$^{-1}$. As the thickness grows from 25 to 30 μm, the corrosion rate has only a slight drop of 4.1 μg cm$^{-2}$ d$^{-1}$ from 34.4 to 30.3 μg cm$^{-2}$ d$^{-1}$. It is implied that the protective effect of increasing the coating thickness gradually tends to become smaller. Fig. 8 depicts the distribution of the Mg ion concentrations after 28 days for the coatings with different thicknesses. Obviously, the thicker the coating, the smaller the ion concentration gradient in the corrosion phase of the alloy matrix, resulting in a slower corrosion rate.

(ii) **The influence of porosity.** The thickness of coating is set to be 30 μm in these simulations. The porosity in different coatings ranges from 0 to 0.3 with an interval of 0.1. Fig. 11 shows that the corresponding average corrosion rate are 25.8, 28.8, 32.7 and 37.1 μg cm$^{-2}$ d$^{-1}$, respectively. It is clear that the corrosion rate increases significantly with increasing porosity. The mass loss rate increases by

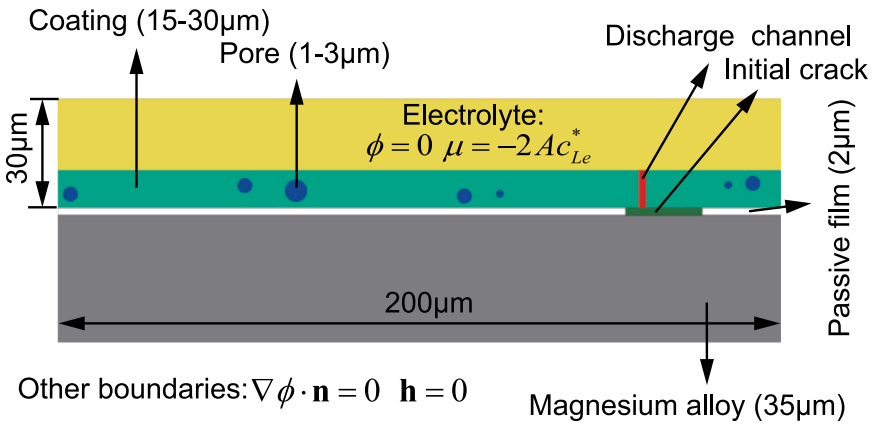


**Fig. 6.** Structure and colour representation of coated magnesium alloy model used for data generation.

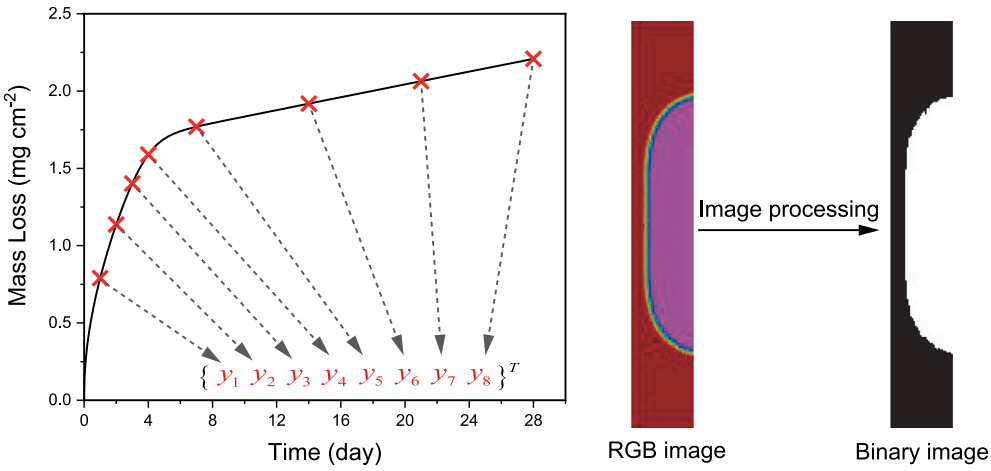


**Fig. 7.** Subsequent processing of the simulation results for generating dataset.

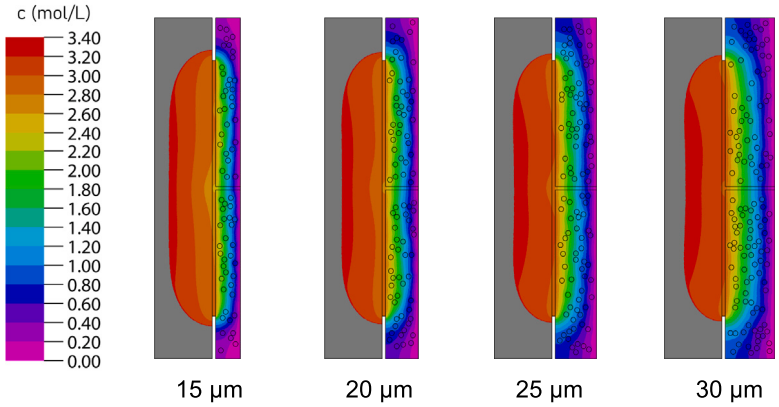


**Fig. 8.** The distribution of the Mg ion concentration after 28 days for PEO coatings with 15% porosity and different thicknesses.

3.0 μg cm$^{-2}$ d$^{-1}$ when the porosity increases from 0 to 0.1 and by 4.4 μg cm$^{-2}$ d$^{-1}$ when the porosity increases from 0.2 to 0.3. The variation of the ion concentration gradient with porosity is demonstrated in Fig. 10, where the higher porosity increases the concentration gradient, resulting in a higher corrosion rate.

### 3.5. Architecture and parametrisation of neural networks

To design the MLP architecture for predicting the corrosion curve, three structural parameters, porosity, coating thickness and the initial crack length of passive film, were used as inputs. The mean square error (MSE) is employed as the loss function for evaluating the performance of different MLP architectures. The learning rate is set at 0.001, and training is conducted over 5000 epochs. A rectified linear unit activation function (ReLU, $\sigma(x) = \max(0, x)$) is used consistently [61]. The testing results of the 2-layer and 3-layer MLP models are presented in Tables 2. Notably, continuously increasing the number of hidden units in 2-layer models does not lead to a stable reduction in testing error. The error reaches its minimum at approximately 48 hidden units, as indicated in Table 2. This suggests that a 2-layer neural network

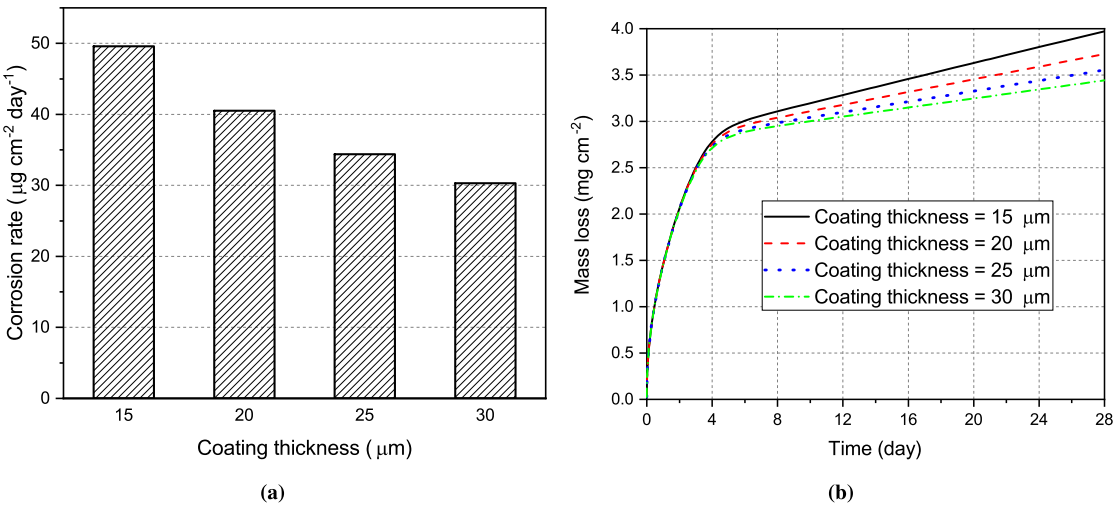


**Fig. 9.** The influence of coating thickness on (a) corrosion rates in Phase II and (b) entire corrosion curves.

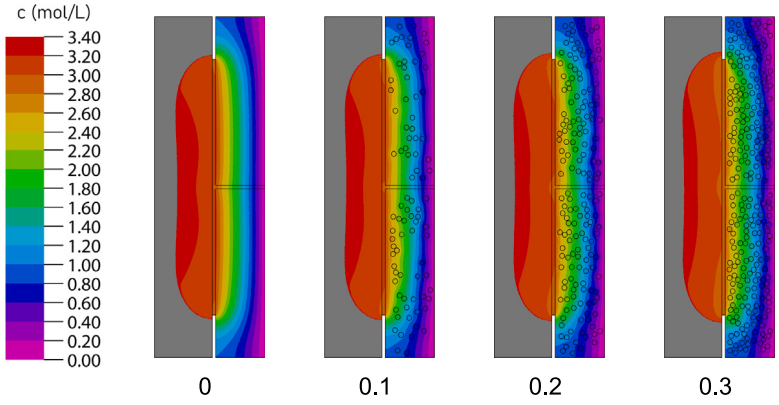


**Fig. 10.** The distribution of Mg ion concentration after 28 days for different porosities of PEO coatings with thickness = 30 μm.

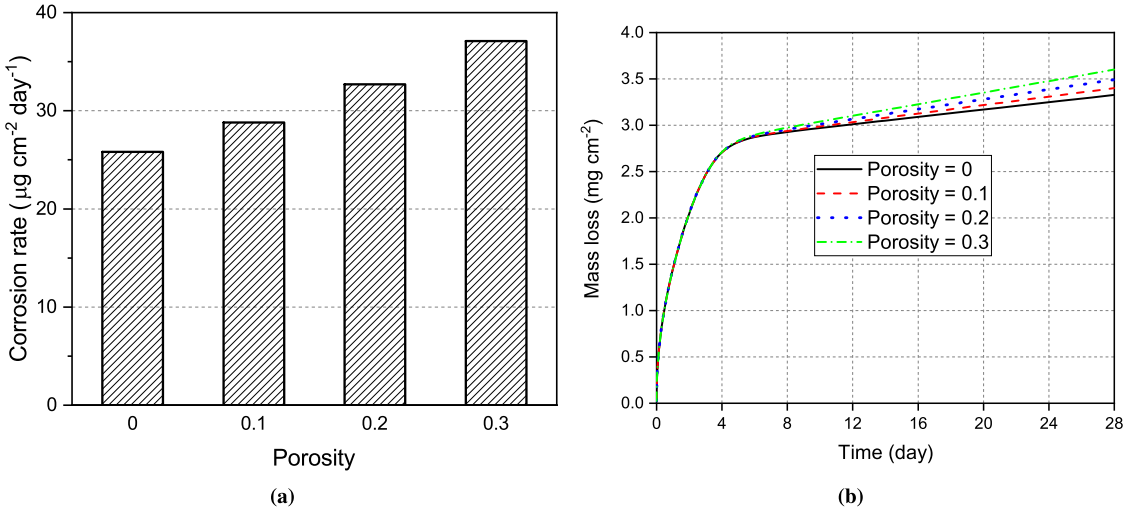


**Fig. 11.** The influence of coating porosity on (a) corrosion rates in Phase II and (b) entire corrosion curves.

performs optimally with a mean relative error of 1.24%. For the 3-layer networks, the testing mean relative error fluctuates around 0.9% with the increase of hidden units in both layers, as shown in . While further enhancements in accuracy may be achievable with additional nodes, the exponential growth in memory and computation cost renders such improvements economically unnecessary. Therefore, considering the prediction accuracy and computational efficiency, the FC network in the following CNN models consists of two hidden layers with 48 nodes and 64 nodes, respectively.

The architecture of the encoder in the CNN models was determined by testing and selecting the architecture configuration with various combinations of convolutional layers and parameters for yielding the

**Table 2**
Mean relative testing error of 2-layer MLP models with different number of hidden units.

| Number of hidden units | 3 | 6 | 12 | 24 | 48 | 96 | 192 | 384 |
|---|---|---|---|---|---|---|---|---|
| Mean relative testing error | 4.36% | 2.51% | 2.06% | 1.41% | 1.24% | 1.25% | 1.33% | 2.05% |

**Table 3**
Mean relative testing error of 3-layer MLP models with different number of hidden units.

| 2nd layer \ 1st layer | 3 | 6 | 12 | 24 | 48 | 96 |
|---|---|---|---|---|---|---|
| 8 | 2.60% | 2.03% | 1.49% | 1.40% | 1.09% | 1.23% |
| 16 | 2.33% | 1.20% | 1.16% | 1.09% | 1.21% | 1.87% |
| 32 | 1.70% | 3.72% | 1.12% | 1.05% | 1.06% | 1.12% |
| 64 | 6.03% | 1.20% | 1.11% | 1.05% | 0.91% | 1.20% |
| 128 | 4.08% | 1.22% | 0.99% | 0.98% | 0.92% | 1.12% |
| 256 | 5.61% | 1.27% | 0.99% | 0.90% | 0.86% | 0.87% |

**Table 4**
Architecture of the encoder and decoder.

| Encoder | | | | | | |
|---|---|---|---|---|---|---|
| Layer | Input | Kernel shape | Number of kernels | Padding | Stride | Output |
| Conv1 | $200 \times 32 \times 3$ | $2 \times 2 \times 3$ | 24 | 1,1 | 1,1 | $201 \times 33 \times 24$ |
| Pool1 | $201 \times 33 \times 24$ | $2 \times 2 \times 1$ | – | – | 2,2 | $100 \times 16 \times 24$ |
| Conv2 | $100 \times 16 \times 24$ | $3 \times 3 \times 24$ | 36 | 1,1 | 3,3 | $33 \times 6 \times 36$ |
| Pool2 | $33 \times 6 \times 36$ | $2 \times 2 \times 1$ | – | – | 2 | $16 \times 3 \times 36$ |
| Conv3 | $16 \times 3 \times 36$ | $2 \times 2 \times 36$ | 42 | 1,1 | 2,2 | $8 \times 2 \times 42$ |
| Pool3 | $8 \times 2 \times 42$ | $2 \times 2 \times 1$ | – | – | 2,2 | $4 \times 1 \times 42$ |
| Decoder | | | | | | |
| ConvTran1 | $4 \times 1 \times 42$ | $3 \times 3 \times 4$ | 672 | – | 1,1 | $6 \times 3 \times 672$ |
| ConvTran2 | $6 \times 3 \times 672$ | $2 \times 3 \times 672$ | 336 | – | 3,2 | $17 \times 7 \times 336$ |
| ConvTran3 | $17 \times 7 \times 336$ | $3 \times 3 \times 336$ | 84 | – | 2,1 | $35 \times 9 \times 84$ |
| ConvTran4 | $35 \times 9 \times 84$ | $3 \times 3 \times 84$ | 21 | – | 2,1 | $71 \times 11 \times 21$ |
| ConvTran5 | $71 \times 11 \times 21$ | $2 \times 2 \times 21$ | 7 | – | 1,1 | $72 \times 12 \times 7$ |
| ConvTran6 | $72 \times 12 \times 7$ | $5 \times 4 \times 7$ | 4 | 4,1 | 3,3 | $210 \times 35 \times 4$ |

best performance. The optimised encoder contains three convolutional layers with convolutional kernel sizes of $2 \times 2, 3 \times 3$, and $2 \times 2$. Each convolution layer is followed by a pooling layer adopting max-pooling with a $2 \times 2$ kernel size and a stride of $2 \times 2$. The number of filters/kernels is chosen to adequately capture the details of the PEO coatings. Although the features of the coating image are easily captured by the kernels in each layer, identifying pattern features along the image edges remains challenging. To address this issue, padding is utilised within the convolution layers to enhance edge features and details. Additionally, padding helps to control the dimensions of the outputs. The design of the decoding network follows the approach proposed by Li et al. [45]. Unlike the encoder, the decoder consists solely of transposed convolution layers. Considering that the input of PEO coating structures and the output of pitting morphologies differ in size and lack explicit structural correspondence, we did not incorporate residual blocks, which are commonly used in previous studies involving image generation to prevent vanishing gradients or preserve structural information [62,63]. The detailed architecture of the decoder network is presented in Table 4. The activation function for all layers is ReLU according the recommendation for deep neural networks [64].

## 4. Computational results and discussion

In this section, we analyse the performance of the three mentioned CNN models based on the validation dataset, which has not been seen by the CNN models during the training phase. To evaluate and compare the two corrosion-curve CNN models, we first demonstrate the testing error evolution in the training phase. Then, the average error of predicted data on each day is calculated to assess the prediction accuracy of each data point. Furthermore, the error distributions for different ranges of the microstructural parameter are analysed to understand the sensitivity of the CNN models to the coating microstructure. Likewise, we evaluate the performance of the CNN model for predicting the corrosion interface by assessing its prediction accuracy and error distributions at four time points.

### 4.1. Performance of the corrosion-curve CNN models

The corrosion-curve single-input CNN and multi-input CNN were both trained for 3000 epochs. The initial learning rate for SICNN was 0.01, while the training of MICNN was started with a learning rate of 0.001. In both training processes, the learning rate was divided by 10 every 300 epochs to achieve a convergence. Fig. 12 shows the evolution of average epoch loss and relative error for training and testing of two corrosion-curve models. To visualise the evolution of the losses more intuitively, logarithmic coordinates are employed. As shown, the mean relative testing error of the SICNN converges to about 2.0% after 300 epochs, while that of the MICNN continues to experience a negligible decline after 2000 epochs. The training results indicate that the MICNN has a superior prediction accuracy compared to the SICNN. Specifically, the final average relative testing error of the MICNN has been reduced to less than 0.5%, which is 77% smaller than that of the SICNN.

Fig. 13(a) demonstrates the absolute and relative errors for the 8 data points predicted by two CNN models based on the validation dataset. It can be noted that the mean absolute prediction error of the single-input CNN for 8 time points is fluctuating upwards, ranging between 6.7 and 18.9 $\mu g\,cm^{-2}$. In contrast, the mean absolute error of the multi-input CNN rises from 1.1 to 8.0 $\mu g\,cm^{-2}$ from Day 1 to Day 28. The mean relative error shows minimal fluctuation, possessing a minimum value 0.45% on Day 2 and a maximum value 0.81% on Day 28. Meanwhile, each phase field simulation on a computer (Intel 10700K, 16 threads) takes approximately 1 h 30 min, whereas SICNN and MICNN can make a prediction within 1.9 ms. With only a minor loss in accuracy, the CNN models reduce the computational cost by over six orders of magnitude compared to the phase field simulation.

#### 4.1.1. Sensitivity of the corrosion-curve CNN models to coating microstructures

The phase field simulations show that the corrosion rate of the coated magnesium alloy in the initial corrosion stage (Phase I) depends

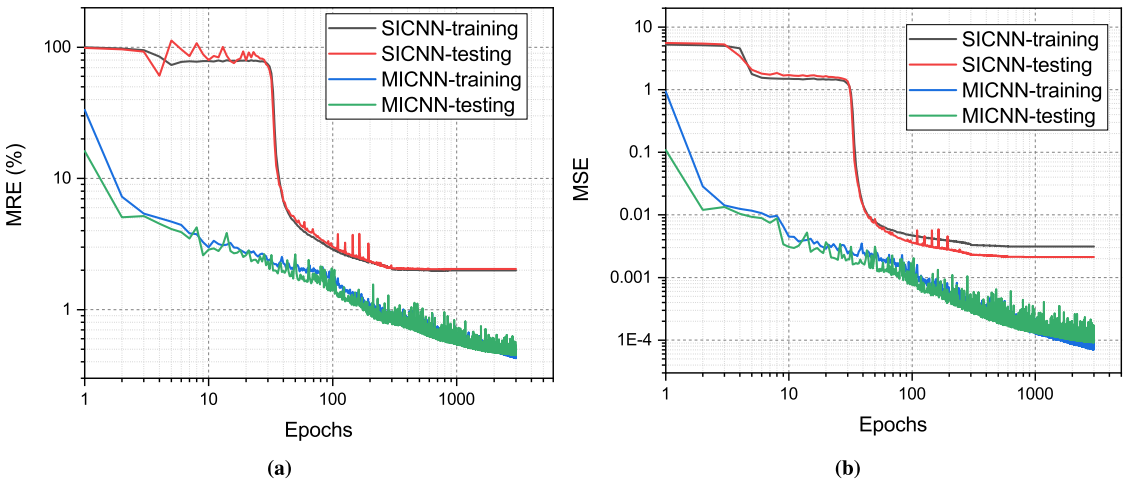


**Fig. 12.** (a) Mean relative error and (b) mean squared error on training and testing data of corrosion-curve CNN models.

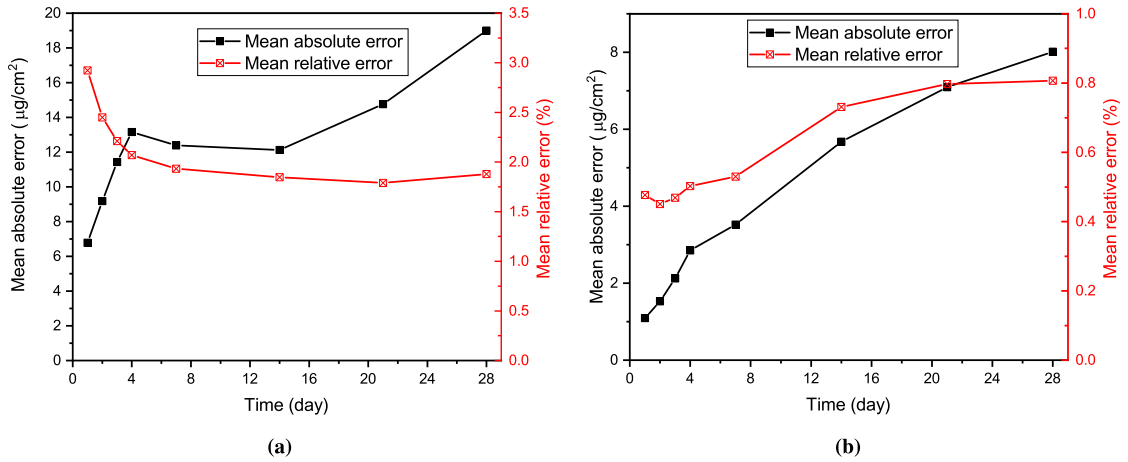


**Fig. 13.** Mean absolute error and mean relative error for each of the 8 data points predicted by (a) the single-input CNN model and (b) the multi-input CNN model in the validation dataset.

almost entirely on the length of the initial crack in the passive film due to the direct contact between the electrolyte and the alloy matrix. After the corrosion products seal the microcracks and pores in the PEO coating (Phase II), the influence of coating thickness and porosity becomes apparent, as discussed in Section 3.4. The analysis of the average relative error of the 8 data points reveals that the prediction accuracy of the regular CNN for Phase I is notably lower than the accuracy for Phase II, while the error distribution of the multi-input CNN exhibits the opposite trend.

To get an insight into the sensitivity of CNN models to microstructural features of coating, the porosity, the initial crack length and the coating thickness in validation set were divided into three groups, respectively: (i) the porosity in the range of [0, 0.1], (0.1, 0.2] and (0.2, 0.3], (ii) the initial crack length in the range of [5, 30 μm], (30, 80 μm] and (80, 150 μm] and (iii) the coating thickness in the range of [15, 20 μm], (20, 25 μm] and (25, 30 μm].

Fig. 14 shows the error distribution of the prediction results produced by the single-input and multi-input CNN model with three different porosity ranges in the validation dataset. Overall, 70% of the predictions from the single-input CNN model have a relative error of less than 2%, while the multi-input CNN can predict the corrosion rate in Phase II with a relative error of less than 1% for nearly 90% data set of the coating microstructures in validation set. It can be observed that the single-input CNN has the highest accuracy in predicting the corrosion curve of coatings with $0.1 < \text{porosity} \leq 0.2$. For the coatings with the porosity in the ranges of [0.0, 0.1], (0.1, 0.2] and (0.2, 0.3], 33%, 47% and 27% of the predictions have a relative error less than 1%, respectively. In contrast, the multi-input CNN model does not exhibit a substantial bias for the three porosity ranges, as the distributions of errors within these porosity intervals are quite consistent. It is indicated that the prediction accuracy of the multi-input CNN is weakly affected by the porosity due to the integration of the porosity as an additional input data.

Compared to the effect of porosity, the initial crack length in the coating affects more significantly the relative error of predictions generated by both CNN models, as shown in Fig. 15. For coatings with a crack length of 5–30 μm, only 18.7% of predictions from the single-input CNN have a relative error of less than 1%, while 60.2% of predictions for coatings with a crack length of 80–150 μm fall into the same error interval. Similarly, 30.1% of the multi-input CNN's predictions for coatings with a crack length of 5–30 μm have an relative error of less than 0.5%, while 93.9% of the predictions for coatings with a crack length of 80–150 μm have the same error. The lower prediction accuracy for coatings with a shorter initial crack length may be attributed to the fact that the corrosion rate in this case is strongly dependent on the local distribution of pores in the vicinity of the initial crack, making it challenging for CNN models to capture this complex correlation accurately.

As shown in Fig. 16(a), it is evident that the single-input CNN model can only provide accurate predictions for coatings with a larger thickness. For coatings with a thickness in the range of 15–20 μm, 24.9% of the single-input CNN's predictions have a relative error less than 1%.

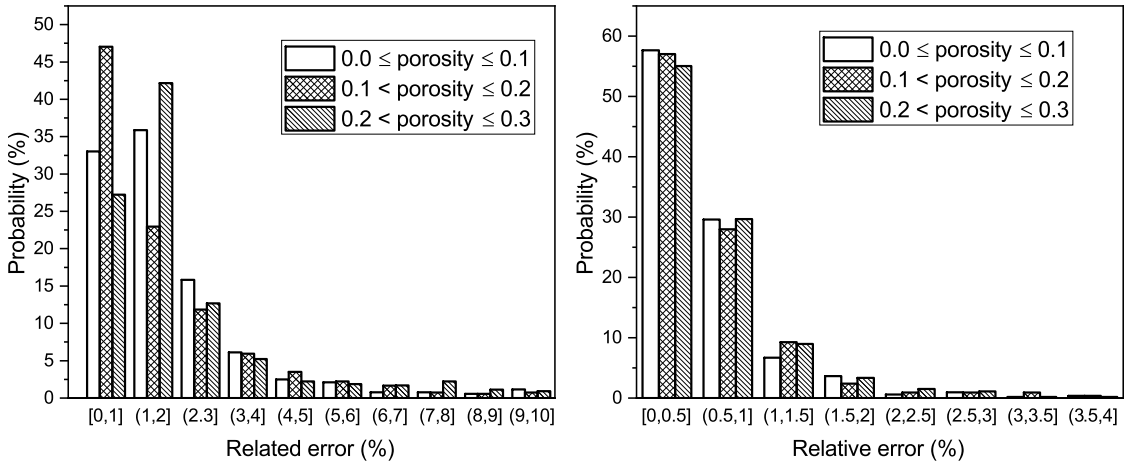


**(a)** Single-input CNN **(b)** Multi-input CNN

**Fig. 14.** Distribution of relative error of the predictions of (a) the single-input CNN model and (b) the multi-input CNN model in different ranges of porosity.

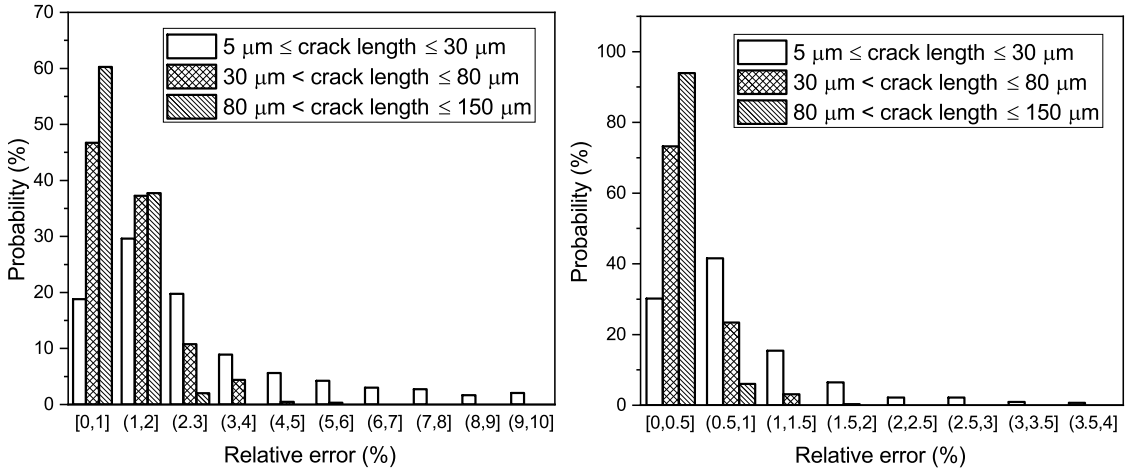


**(a)** Single-input CNN **(b)** Multi-input CNN

**Fig. 15.** Distribution of relative error of the predictions of (a) the single-input CNN model and (b) the multi-input CNN model in different ranges of initial crack length.

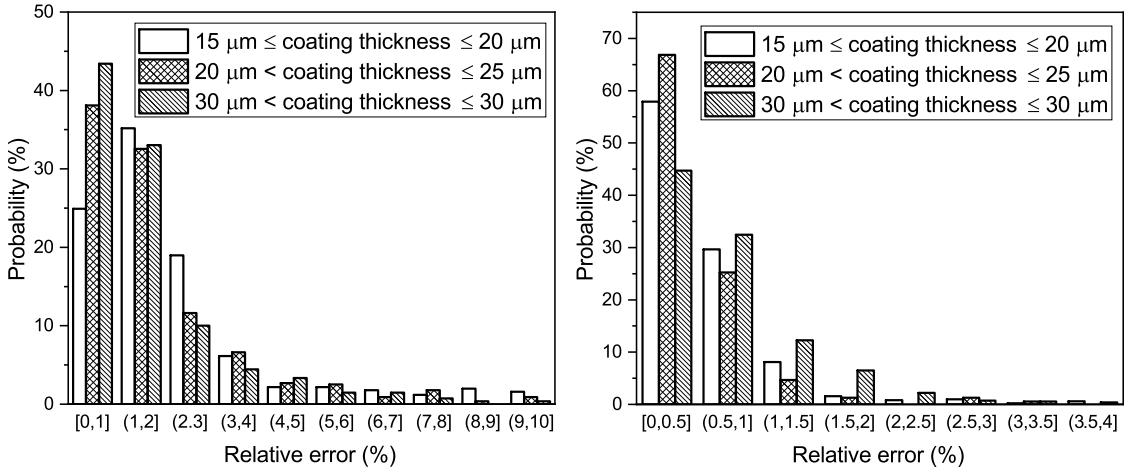


**(a)** Single-input CNN **(b)** Multi-input CNN

**Fig. 16.** Distribution of relative error of the predictions of (a) the single-input CNN model and (b) the multi-input CNN model in different ranges of coating thickness.

**Table 5**
The evolution of mass loss and the average corrosion rate in Phase II predicted by phase field simulations and the corrosion-curve CNN models for three coated magnesium alloy models with different pore distributions shown in Fig. 17.

| Mass loss per area ($mg\,cm^{-2}$) | | | | | | | Average corrosion rate ($\mu g\,cm^{-2}\,d^{-1}$) |
|---|---|---|---|---|---|---|---|
| Number of days | | 4 | 7 | 14 | 21 | 28 | in Phase II |
| Phase field simulation | A | 1.22 | 1.28 | 1.39 | 1.49 | 1.59 | 15.4 |
| | B | 1.22 | 1.30 | 1.41 | 1.53 | 1.65 | 17.9 |
| | C | 1.22 | 1.31 | 1.46 | 1.61 | 1.76 | 22.5 |
| Single-input CNN prediction | A | 1.20 | 1.29 | 1.41 | 1.53 | 1.65 | 18.9 |
| | B | 1.21 | 1.29 | 1.42 | 1.55 | 1.67 | 19.1 |
| | C | 1.22 | 1.31 | 1.44 | 1.57 | 1.71 | 20.4 |
| Multi-input CNN prediction | A | 1.22 | 1.29 | 1.40 | 1.51 | 1.63 | 17.1 |
| | B | 1.22 | 1.30 | 1.41 | 1.53 | 1.65 | 17.9 |
| | C | 1.22 | 1.31 | 1.45 | 1.58 | 1.71 | 20.4 |

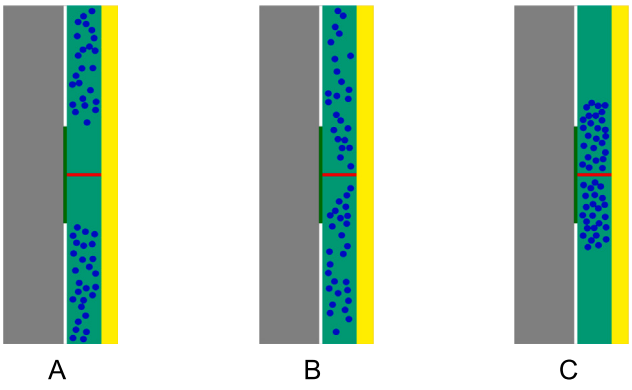


**Fig. 17.** Three coated magnesium alloy models with the same coating thickness, porosity and initial crack length in passive film.

In the range of 25–30 μm, 43.4% of the single-input CNN's predictions have a relative error less than 1%. Setting the coating thickness as a microstructural parameter for additional inputs improves the prediction accuracy of the multi-input CNN. As a result, the multi-input CNN model yields the better prediction results with a higher probability of the relative error less than 0.5% for coatings with different thickness ranges, as demonstrated in Fig. 16(b).

#### 4.1.2. Encoder performance in extracting coating structure features

As mentioned in Section 4.1.1, the distribution of pores near the initial crack in the passive film can significantly impact on the corrosion rate of the coated magnesium alloy in Phase II. However, the porosity as a macroscopic parameter cannot capture the detailed microstructural features of coating. Especially when the initial crack in the passive film is very small, the distribution of pores around the crack plays a crucial role in the corrosion process. Quantifying this location-specific information of microstructures can be challenging for the CNN models. Therefore, three coatings with the same coating thickness (20 μm), initial crack length (60 μm), and porosity (0.15) but different pore distributions shown in Fig. 17 are used to test the ability of the current encoder in the CNN models for extracting the local microstructural features. The corresponding corrosion data in Phase II obtained from phase field simulations and the corrosion-curve CNN models are listed in Table 5. It is shown that average the corrosion rate (22.5 $\mu g\,cm^{-2}\,d^{-1}$) in Phase II for Model C is 46.1% higher than that of Model A (15.4 $\mu g\,cm^{-2}\,d^{-1}$) according to the phase field simulation results. Similarly, the proposed CNN models are able to capture this difference of the corrosion rate in different coating models, although the accuracy is slightly reduced. It is worth noting that the multi-input CNN produces results closer to the ground truth than the single-input CNN. This comparison demonstrates that the encoder in CNN models can successfully correlate the local microstructural features of the coating to the corrosion behaviour of coated magnesium alloys.

### 4.2. Performance of the corrosion-interface CNN model

The corrosion-interface CNN model was trained for 5000 epochs with constant learning rate 0.001. The loss of train dataset and the loss of test dataset during training are demonstrated in Fig. 18(a). Unlike the training of previous two corrosion-curve CNN models with an oscillation of the testing loss during training, the testing loss of the corrosion-interface CNN model decreases smoothly during training and converges quickly to 0.002. Considering the computational cost, each prediction of the corrosion-interface CNN model can be produced within 24 ms. The error distribution analysis of the corrosion interface predictions illustrated in Fig. 18(b) shows that the error increases as the corrosion process proceeds. For the interface after 1-day corrosion, more than 90% of predictions have a relative error of less than 0.6%, while only 74% of predictions for the interface after 28-day corrosion have a relative error of less than 1.2%. It is implied that it becomes increasingly challenging to predict it with high precision, as the corrosion interface evolves and becomes more complex. The predicted results from the validation dataset demonstrate the interface evolution and their corresponding ground truth, as shown in Fig. 19. The 1% mean relative error indicates almost indistinguishable differences between the prediction and the ground truth. Moreover, the temporal evolution of the corrosion interface can be captured by the CNN model with a good accuracy.

## 5. Conclusion

In this work, we have developed a CNN based deep learning framework for predicting the temporal evolution of the mass loss and the pit morphology during the corrosion process of coated magnesium alloys. The utilised phase field model for pitting corrosion is formulated based on the stationarity principle of rate-type potential functional. The phase field simulations with different coating microstructures were used to generate corrosion datasets for training and validating the CNN models. The presented deep learning framework encompasses the generation of coating microstructures, data preprocessing, dataset construction, and optimal architecture search of neural networks. The hybrid approach of phase field modelling and machine learning for predicting the corrosion behaviour of biodegradable magnesium alloy-coating system has been applied to the PEO coated magnesium alloy WE43MEO. Through the detailed analysis and evaluation of phase field simulations and the neural networks' performance, we draw the following conclusions:

- The present phase field simulation can quantitatively capture the corrosion behaviour of coated magnesium alloys. The simulation results reveal that the corrosion rate in the initial corrosion stage are strongly affected by the initial crack in the passive film and discharge channels in the coating, which enable direct contact between the electrolyte and the alloy matrix. As the corrosion products seal the microcracks and pores in the coating, the influence of coating thickness and porosity becomes apparent for the corrosion behaviour of magnesium alloys.

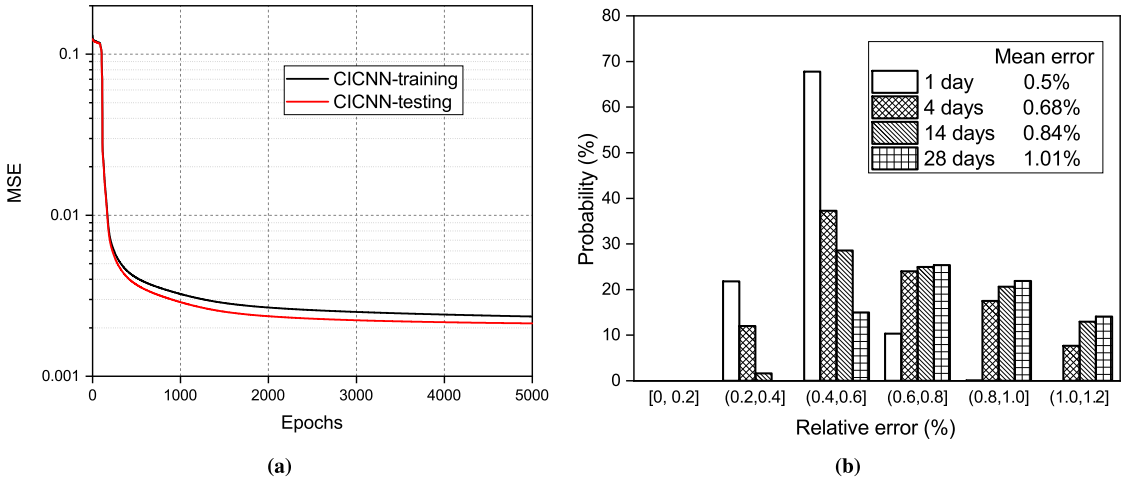


**Fig. 18.** (a) Mean squared error on training and testing data of the corrosion-interface CNN and (b) mean relative error distribution of interfaces predicted by the corrosion-interface CNN based on the validation dataset.

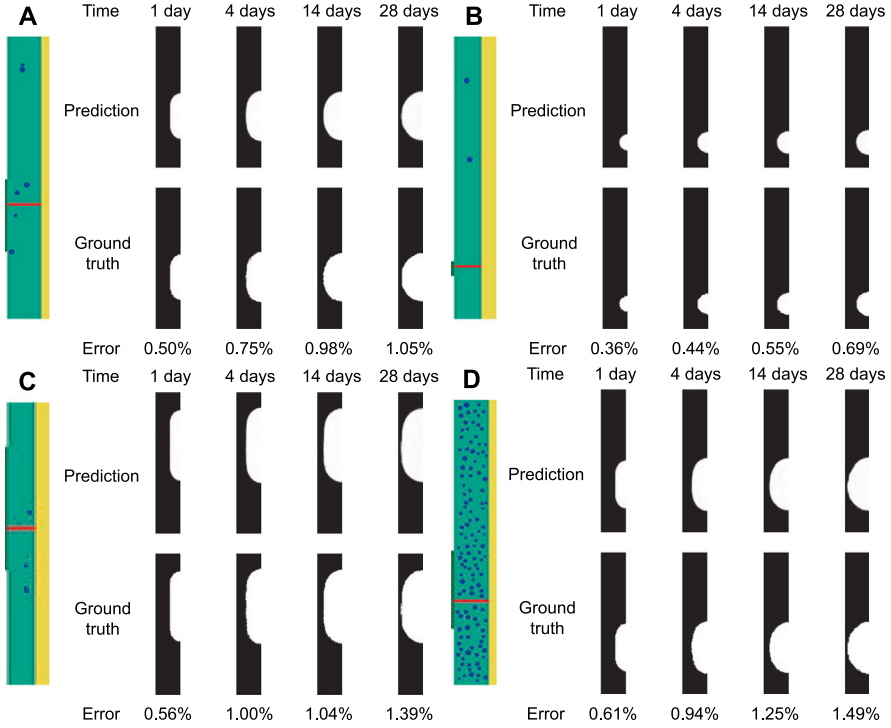


**Fig. 19.** The evolutions of corrosion interfaces of four models with different coating structures. The examples are selected in the validation dataset to show the prediction performance for different structural parameters. For each configuration, predicted results, the ground truth results and errors are shown from top to bottom.

- The corrosion-curve CNN models demonstrate reliable convergence during the training phase. The incorporation of structural parameters of coating features significantly improved the prediction accuracy of the multi-input architecture, compared to the traditional single-input CNN model. Microstructural sensitivity analysis reveals that the multi-input CNN model is less sensitive to the coating microstructure.
- The prediction ability of the multi-input CNN model for the coating with different pore distributions confirms that the encoder has effectively learned the local microstructural features from the images of coatings.
- The binary images used in the encoder–decoder architecture of the CNN models result in an accurate prediction of corrosion morphology with a relative error of less than 1%.
- In comparison to phase field simulations, the machine learning based approach significantly reduces the computational cost by over six orders while maintaining high accuracy.

## CRediT authorship contribution statement

**Songyun Ma:** Writing – original draft, Visualization, Validation, Project administration, Methodology, Investigation, Funding acquisition, Formal analysis, Data curation, Conceptualization. **Dawei Zhang:** Writing – review & editing, Visualization, Validation, Methodology, Investigation, Data curation, Conceptualization. **Peilei Zhang:** Writing – review & editing, Validation, Methodology, Formal analysis. **Bernd Markert:** Writing – review & editing, Resources, Conceptualization.

## Declaration of competing interest

The authors declare that they have no known competing financial interests or personal relationships that could have appeared to influence the work reported in this paper.

## Acknowledgements

This research was supported by the Federal Ministry of Education and Research of Germany in the framework of RePlaSys (Project number FKZ 13GW0352B). Mr. Dawei Zhang would like to acknowledge the research funding from the China Scholarship Council (Reference No. 202108080318).

## Data availability

Data will be made available on request.

## References

[1] P. Chakraborty Banerjee, S. Al-Saadi, L. Choudhary, S.E. Harandi, R. Singh, Magnesium implants: Prospects and challenges, Materials 12 (1) (2019) 136.
[2] T.S. Narayanan, I.S. Park, M.H. Lee, Strategies to improve the corrosion resistance of microarc oxidation (MAO) coated magnesium alloys for degradable implants: Prospects and challenges, Prog. Mater. Sci. 60 (2014) 1–71.
[3] F. Peng, H. Li, D. Wang, P. Tian, Y. Tian, G. Yuan, D. Xu, X. Liu, Enhanced corrosion resistance and biocompatibility of magnesium alloy by Mg–Al-layered double hydroxide, ACS Appl. Mater. Interfaces 8 (51) (2016) 35033–35044.
[4] M. Fouladi, A. Amadeh, Effect of phosphating time and temperature on microstructure and corrosion behavior of magnesium phosphate coating, Electrochim. Acta 106 (2013) 1–12.
[5] H.M. Wong, K.W. Yeung, K.O. Lam, V. Tam, P.K. Chu, K.D. Luk, K.M. Cheung, http://dx.doi.org/10.1016/j.biomaterials.2009.11.111.
[6] C. Blawert, W. Dietzel, E. Ghali, G. Song, Anodizing treatments for magnesium alloys and their effect on corrosion resistance in various environments, Adv. Eng. Mater. 8 (6) (2006) 511–533, http://dx.doi.org/10.1002/adem.200500257.
[7] P. Volovitch, J. Masse, A. Fabre, L. Barrallier, W. Saikaly, Microstructure and corrosion resistance of magnesium alloy ZE41 with laser surface cladding by Al–Si powder, Surf. Coat. Technol. 202 (20) (2008) 4901–4914.
[8] C.-A. Chen, S.-Y. Jian, C.-H. Lu, C.-Y. Lee, S.L. Aktuğ, M.-D. Ger, Evaluation of microstructural effects on corrosion behavior of AZ31B magnesium alloy with a MAO coating and electroless Ni-P plating, J. Mater. Res. Technol. 9 (6) (2020) 13902–13913.
[9] P. Tong, Y. Sheng, R. Hou, M. Iqbal, L. Chen, J. Li, Recent progress on coatings of biomedical magnesium alloy, Smart Mater. Med. 3 (2022) 104–116.
[10] D. Gastaldi, V. Sassi, L. Petrini, M. Vedani, S. Trasatti, F. Migliavacca, Continuum damage model for bioresorbable magnesium alloy devices - Application to coronary stents, J. Mech. Behav. Biomed. Mater. 4 (3) (2011) 352–365.
[11] J.A. Grogan, B.J. O'Brien, S.B. Leen, P.E. McHugh, A corrosion model for bioabsorbable metallic stents, Acta Biomater. 7 (9) (2011) 3523–3533.
[12] J.A. Grogan, S.B. Leen, P.E. McHugh, Optimizing the design of a bioabsorbable metal stent using computer simulation methods, Biomaterials 34 (33) (2013) 8049–8060.
[13] S. Ma, B. Zhou, B. Markert, Numerical simulation of the tissue differentiation and corrosion process of biodegradable magnesium implants during bone fracture healing, ZAMM Z. Angew. Math. Mech. 98 (12) (2018) 2223–2238.
[14] E. Gazenbiller, S. Mansoor, N. Konchakova, M. Serdechnova, M.L. Zheludkevich, C. Blawert, D. Höche, Computational damage modelling of PEO coated extruded magnesium tested in slow strain rate configuration, Surf. Coat. Technol. 446 (2022) 128758.
[15] K. van Gaalen, C. Quinn, M. Weiler, F. Gremse, F. Benn, P.E. McHugh, T.J. Vaughan, A. Kopp, Predicting localised corrosion and mechanical performance of a PEO surface modified rare earth magnesium alloy for implant use through in-silico modelling, Bioactive Mater. 26 (2023) 437–451.
[16] J. Grogan, S. Leen, P. McHugh, A physical corrosion model for bioabsorbable metal stents, Acta Biomater. 10 (5) (2014) 2313–2322.
[17] J. Sanz-Herrera, E. Reina-Romo, A. Boccaccini, In silico design of magnesium implants: Macroscopic modeling, J. Mech. Behav. Biomed. Mater. 79 (2018) 181–188.
[18] Z. Shen, M. Zhao, D. Bian, D. Shen, X. Zhou, J. Liu, Y. Liu, H. Guo, Y. Zheng, Predicting the degradation behavior of magnesium alloys with a diffusion-based theoretical model and in vitro corrosion testing, J. Mater. Sci. Technol. 35 (7) (2019) 1393–1402, http://dx.doi.org/10.1016/j.jmst.2019.02.004.
[19] B. Zeller-Plumhoff, T. AlBaraghtheh, D. Höche, R. Willumeit-Römer, Computational modelling of magnesium degradation in simulated body fluid under physiological conditions, J. Magnesium Alloys 10 (4) (2022) 965–978.
[20] W. Mai, S. Soghrati, R.G. Buchheit, A phase field model for simulating the pitting corrosion, Corros. Sci. 110 (2016) 157–166, http://dx.doi.org/10.1016/j.corsci.2016.04.001.
[21] C. Tsuyuki, A. Yamanaka, Y. Ogimoto, Phase-field modeling for pH-dependent general and pitting corrosion of iron, Sci. Rep. 8 (1) (2018) http://dx.doi.org/10.1038/s41598-018-31145-7.
[22] T.Q. Ansari, Z. Xiao, S. Hu, Y. Li, J.L. Luo, S.Q. Shi, Phase-field model of pitting corrosion kinetics in metallic materials, npj Comput. Mater. 4 (1) (2018) 1–9, http://dx.doi.org/10.1038/s41524-018-0089-4.
[23] B. Zhou, Y. Heider, S. Ma, B. Markert, Phase-field-based modelling of the gelation process of biopolymer droplets in 3D bioprinting, Comput. Mech. 63 (6) (2019) 1187–1202.
[24] W. Mai, S. Soghrati, New phase field model for simulating galvanic and pitting corrosion processes, Electrochim. Acta 260 (2018) 290–304.
[25] S. Kovacevic, W. Ali, E. Martínez-Pañeda, J. LLorca, Phase-field modeling of pitting and mechanically-assisted corrosion of Mg alloys for biomedical applications, Acta Biomater. 164 (2023) 641–658.
[26] D. Zhang, S. Ma, J. Nachtsheim, S. Zhang, B. Markert, A variational phase-field framework for multiphysics modelling of degradation and stress corrosion cracking in biodegradable magnesium alloys, J. Mech. Phys. Solids 190 (2024) 105694, http://dx.doi.org/10.1016/j.jmps.2024.105694, URL https://www.sciencedirect.com/science/article/pii/S0022509624001601.
[27] K. Yang, Y. Cao, Y. Zhang, S. Fan, M. Tang, D. Aberg, B. Sadigh, F. Zhou, Self-supervised learning and prediction of microstructure evolution with convolutional recurrent neural networks, Patterns 2 (5) (2021).
[28] P. Wu, A.S. Iquebal, K. Ankit, Emulating microstructural evolution during spinodal decomposition using a tensor decomposed convolutional and recurrent neural network, Comput. Mater. Sci. 224 (2023) 112187.
[29] L.B. Coelho, D. Zhang, Y. Van Ingelgem, D. Steckelmacher, A. Nowé, H. Terryn, Reviewing machine learning of corrosion prediction in a data-oriented perspective, npj Mater. Degrad. 6 (1) (2022) 8.
[30] O.I. Abiodun, A. Jantan, A.E. Omolara, K.V. Dada, N.A. Mohamed, H. Arshad, State-of-the-art in artificial neural network applications: A survey, Heliyon 4 (11) (2018).
[31] Z. Li, F. Liu, W. Yang, S. Peng, J. Zhou, A survey of convolutional neural networks: analysis, applications, and prospects, IEEE Trans. Neural Netw. Learn. Syst. 33 (12) (2021) 6999–7019.
[32] A. Frankel, K. Tachida, R. Jones, Prediction of the evolution of the stress field of polycrystals undergoing elastic-plastic deformation with a hybrid neural network model, Mach. Learn.: Sci. Technol. 1 (3) (2020) 035005.
[33] H. Wu, W.-Z. Fang, Q. Kang, W.-Q. Tao, R. Qiao, Predicting effective diffusivity of porous media from images by deep learning, Sci. Rep. 9 (1) (2019) 1–12.
[34] D.W. Abueidda, M. Almasri, R. Ammourah, U. Ravaioli, I.M. Jasiuk, N.A. Sobh, Prediction and optimization of mechanical properties of composites using convolutional neural networks, Compos. Struct. 227 (2019) 111264.
[35] J. Wu, X. Yin, H. Xiao, Seeing permeability from images: fast prediction with convolutional neural networks, Science bulletin 63 (18) (2018) 1215–1222.
[36] K. Pierson, A. Rahman, A.D. Spear, Predicting microstructure-sensitive fatigue-crack path in 3D using a machine learning framework, JOM 71 (8) (2019) 2680–2694.
[37] M. Chaaban, Y. Heider, W. Sun, B. Markert, A machine-learning supported multi-scale LBM-TPM model of unsaturated, anisotropic, and deformable porous materials, Int. J. Numer. Anal. Methods Geomech. 48 (4) (2024) 889–910.
[38] Y. Guo, M. Sun, W. Zhang, L. Wang, Machine learning in enhancing corrosion resistance of magnesium alloys: A comprehensive review, Metals 13 (10) (2023) 1790.
[39] A. Moses, D. Chen, P. Wan, S. Wang, Prediction of electrochemical corrosion behavior of magnesium alloy using machine learning methods, Mater. Today Commun. 37 (2023) 107285.
[40] E.J. Schiessler, T. Würger, S.V. Lamaka, R.H. Meißner, C.J. Cyron, M.L. Zheludkevich, C. Feiler, R.C. Aydin, Predicting the inhibition efficiencies of magnesium dissolution modulators using sparse machine learning models, npj Comput. Mater. 7 (1) (2021) 193.
[41] Y. Wang, T. Xie, Q. Tang, M. Wang, T. Ying, H. Zhu, X. Zeng, High-throughput calculations combining machine learning to investigate the corrosion properties of binary Mg alloys, J. Magnesium Alloys (2022).
[42] A. Maqbool, A. Khalad, N.Z. Khan, Prediction of corrosion rate for friction stir processed WE43 alloy by combining PSO-based virtual sample generation and machine learning, J. Magnesium Alloys (2024).
[43] J. Masci, U. Meier, D. Cireşan, J. Schmidhuber, Stacked convolutional auto-encoders for hierarchical feature extraction, in: Artificial Neural Networks and Machine Learning–ICANN 2011: 21st International Conference on Artificial Neural Networks, Espoo, Finland, June 14-17, 2011, Proceedings, Part I 21, Springer, 2011, pp. 52–59.
[44] J. Geng, J. Fan, H. Wang, X. Ma, B. Li, F. Chen, High-resolution SAR image classification via deep convolutional autoencoders, IEEE Geosci. Remote Sens. Lett. 12 (11) (2015) 2351–2355.
[45] A. Li, R. Chen, A.B. Farimani, Y.J. Zhang, Reaction diffusion system prediction based on convolutional neural network, Sci. Rep. 10 (1) (2020) 1–9.

[46] M.A. Nielsen, Neural Networks and Deep Learning, vol. 25, Determination press San Francisco, CA, USA, 2015.
[47] I. Goodfellow, Y. Bengio, A. Courville, Y. Bengio, Deep Learning, vol. 1, (2) MIT press Cambridge, 2016.
[48] D.E. Rumelhart, G.E. Hinton, R.J. Williams, Learning representations by back-propagating errors, Nature 323 (6088) (1986) 533–536.
[49] J. Nachtsheim, S. Ma, J. Burja, B. Markert, In vitro evaluation of stress corrosion cracking susceptibility of PEO-coated rare-earth magnesium alloy WE43, Surf. Coat. Technol. 477 (2024) 130391.
[50] J. Nachtsheim, J. Burja, S. Ma, B. Markert, Long-term in vitro corrosion of biodegradable WE43 magnesium alloy in DMEM, Metals 12 (12) (2022).
[51] J. Nachtsheim, S. Ma, J. Burja, B.Š. Batič, B. Markert, Tuning the long-term corrosion behaviour of biodegradable WE43 magnesium alloy by PEO coating, Surf. Coat. Technol. 474 (2023) 130115.
[52] M. Ascencio, M. Pekguleryuz, S. Omanovic, An investigation of the corrosion mechanisms of WE43 Mg alloy in a modified simulated body fluid solution: The influence of immersion time, Corros. Sci. 87 (2014) 489–503.
[53] J.W. Cahn, J.E. Hilliard, Free energy of a nonuniform system. I. Interfacial free energy, J. Chem. Phys. 28 (2) (1958) 258–267.
[54] W. Mai, S. Soghrati, R.G. Buchheit, A phase field model for simulating the pitting corrosion, Corros. Sci. 110 (2016) 157–166.
[55] J. Yang, C. Blawert, S.V. Lamaka, D. Snihirova, X. Lu, S. Di, M.L. Zheludkevich, Corrosion protection properties of inhibitor containing hybrid PEO-epoxy coating on magnesium, Corros. Sci. 140 (2018) 99–110.
[56] Y. Li, F. Lu, H. Li, W. Zhu, H. Pan, G. Tan, Y. Lao, C. Ning, G. Ni, Corrosion mechanism of micro-arc oxidation treated biocompatible AZ31 magnesium alloy in simulated body fluid, Progr. Nat. Sci.: Mater. Int. 24 (5) (2014) 516–522.
[57] J. Lu, X. He, H. Li, R. Song, Microstructure and corrosion resistance of PEO coatings formed on KBM10 Mg alloy pretreated with nd (NO3) 3, Materials 11 (7) (2018) 1062.
[58] A. Fattah-Alhosseini, R. Chaharmahali, K. Babaei, M. Nouri, M.K. Keshavarz, M. Kaseem, A review of effective strides in amelioration of the biocompatibility of PEO coatings on Mg alloys, J. Magnesium Alloys 10 (9) (2022) 2354–2383.
[59] Z. Shen, M. Zhao, D. Bian, D. Shen, X. Zhou, J. Liu, Y. Liu, H. Guo, Y. Zheng, Predicting the degradation behavior of magnesium alloys with a diffusion-based theoretical model and in vitro corrosion testing, J. Mater. Sci. Technol. 35 (7) (2019) 1393–1402.
[60] L. An, Y. Ma, Y. Liu, L. Sun, S. Wang, Z. Wang, Effects of additives, voltage and their interactions on PEO coatings formed on magnesium alloys, Surf. Coat. Technol. 354 (2018) 226–235.
[61] K. He, X. Zhang, S. Ren, J. Sun, Deep residual learning for image recognition, in: Proceedings of the IEEE Conference on Computer Vision and Pattern Recognition, 2016, pp. 770–778.
[62] Z. Nie, H. Jiang, L.B. Kara, Stress field prediction in cantilevered structures using convolutional neural networks, J. Comput. Inf. Sci. Eng. 20 (1) (2020) 011002.
[63] D.W. Abueidda, S. Koric, N.A. Sobh, H. Sehitoglu, Deep learning for plasticity and thermo-viscoplasticity, Int. J. Plast. 136 (2021) 102852.
[64] A.K. Bhoi, P.K. Mallick, C.-M. Liu, V.E. Balas, Bio-Inspired Neurocomputing, vol. 310, Springer, 2021.